

Article

Stabilizing Li-Rich Layered Cathode Materials Using a LiCoMnO₄ Spinel Nanolayer for Li-Ion Batteries

Hsiu-Fen Lin *, Si-Ting Cheng, De-Zhen Chen, Nian-Ying Wu, Zong-Xiao Jiang and Chun-Ting Chang

Department of Materials Science and Engineering, National Formosa University, Yunlin 632301, Taiwan

* Correspondence: tiffany1030@nfu.edu.tw

Abstract: Lithium-rich cathodes have excess lithium in the transition metal layer and exhibit an extremely high specific capacity and good energy density. However, they still have some disadvantages. Here, we propose LiCoMnO₄, a new nanolayer coating material with a spinel structure, to modify the surface of lithium cathode oxide (Li_{7/6}Mn_{1/2}Ni_{1/6}Co_{1/6}O₂) with a layered structure. The designed cathode with nanolayer spinel coating delivers an excellent reversible capacity, outstanding rate capability, and superior cycling ability whilst exhibiting discharge capacities of 300, 275, 220, and 166 mAh g⁻¹ at rates of 0.1 C at 2.0–4.8 V formation and 0.1, 1, and 5 C, respectively, between 2.0 and 4.6 V. The cycling ability and voltage fading at a high operational voltage of 4.9 V were also investigated, with results showing that the nanolayer spinel coating can depress the surface of the lithium cathode oxide layer, leading to phase transformation that enhances the electrochemical performance.

Keywords: layered cathode; nanolayer spinel coating; cycling ability; rate capability



Citation: Lin, H.-F.; Cheng, S.-T.; Chen, D.-Z.; Wu, N.-Y.; Jiang, Z.-X.; Chang, C.-T. Stabilizing Li-Rich Layered Cathode Materials Using a LiCoMnO₄ Spinel Nanolayer for Li-Ion Batteries. *Nanomaterials* **2022**, *12*, 3425. <https://doi.org/10.3390/nano12193425>

Academic Editor: Carlos Miguel Costa

Received: 2 September 2022

Accepted: 23 September 2022

Published: 29 September 2022

Publisher's Note: MDPI stays neutral with regard to jurisdictional claims in published maps and institutional affiliations.



Copyright: © 2022 by the authors. Licensee MDPI, Basel, Switzerland. This article is an open access article distributed under the terms and conditions of the Creative Commons Attribution (CC BY) license (<https://creativecommons.org/licenses/by/4.0/>).

1. Introduction

With the intensification of climate change and environmental pollution, lithium-ion batteries (LIBs) are being increasingly pursued to power electric vehicles (EVs) and store renewable energy [1–3]. A safe, long cycle life with higher energy density and good chemical performance is desired for LIBs. Increasing the capacity of the cathode and the charging voltage of the cells are potential methods for achieving this. A lithium-rich cathode with excess lithium in the transition metal layer shows an extraordinarily high specific capacity after an irreversible oxygen release activation process at approximately 4.5 V, which may be a promising solution for producing next-generation cathode materials. However, owing to the shortcomings of the low initial Coulombic efficiency, poor rate capability, and voltage attenuation upon cycling, lithium-rich cathodes are difficult to commercialize [4–7].

Recently, the disadvantages of lithium-rich cathodes were found to be associated with the poor mass transport of the rearranged surface once the activation of Li₂MnO₃ exceeds 4.5 V [8]. In addition, the elimination of the oxygen atom and Li⁺ vacancies from the layered lattice, which decreases the number of sites for insertion and extraction of Li⁺ in subsequent cycles, is the reason for the irreversible capacity [9]. These materials also possess fragile surface properties at high potentials, can experience electrolytic erosion, and may induce the dissolution of transition metal ions [10–12]. Recently, it was reported that surface modification and bulk doping could potentially overcome these issues.

The surface modification of cathode materials by metal oxide layers such as Al₂O₃, NbO₅, Ta₂O₅, ZrO₂, and ZnO [13–18] can decrease side reactions at the electrode–electrolyte interface, but this usually has a negative impact on the rate capability due to the slow Li⁺ or electron–conductivity of the coating layer [19,20]. Recent studies have suggested that coating cathode materials with a layer of electron conductors or Li⁺ conductors, such as carbon [21], AlF₃ [22], LiNiPO₄ [23], Li₂ZrO₃ [24], or LiMgPO₄ [25], can enhance the rate

capability to some extent, as these can promote charge transfer or Li^+ diffusion from the surface of the electrode material.

Spinel-type $\text{LiNi}_x\text{Mn}_{2-x}\text{O}_4$ ($0 < x < 0.5$) oxides exhibit great potential as high-power cathode materials for LIBs [17,26,27] because of their high Li^+ ionic and electronic conductivities [28], high voltage, low cost, and low toxicity. Presently, spinel oxides are a considerable choice to encapsulate Ni-rich layered oxides for identical cubic close-packed arrays [29,30]. Yan et al. [31] designed a composition of a Ni-rich layered core and a $\text{LiNi}_{0.5}\text{Mn}_{1.5}\text{O}_4$ -like spinel shell. The heterostructure, with a low degree of Ni^{2+} and Li^+ disordering, can afford a stable structure framework and high-efficiency paths for the diffusion of lithium ions. Min et al. [32] proposed novel particles, the spinel interphase of which is coherent with the surface of the $\text{LiNi}_{0.9}\text{Co}_{0.06}\text{Mn}_{0.03}\text{O}_2$ (NCM) cathode. The spinel-coated NCM structures outperformed the bare sample in terms of the capacity retention rate and rate capability: they conserved more than 90% of the initial capacity at 1C for up to 50 cycles. After cycling, the crack generation was significantly reduced in the secondary particles of the coated structures compared to that of the bare sample.

In addition, some studies have combined the advantages of lithium-rich cathodes and spinel materials to enhance electrochemical performance in terms of kinetics, energetics, and core material stability [33–35]. In a study by Choi et al. [36], Li-rich composite oxides were synthesized by doping LiMn_2O_4 , $\text{LiNi}_{0.5}\text{Mn}_{1.5}\text{O}_4$, and $\text{LiCo}_{0.5}\text{Mn}_{1.5}\text{O}_4$. Of the various composites created, the $\text{LiNi}_{0.5}\text{Mn}_{1.5}\text{O}_4$ -embedded sample showed lower formation energy as determined by first-principles calculation [37,38]. Furthermore, the Li-rich oxide composite formed by doping the optimal spinel, $\text{LiNi}_{0.5}\text{Mn}_{1.5}\text{O}_4$, exhibited the best cycling performance with little voltage decay when used in a cylindrical 18650-type full cell. Wu et al. [39] developed a lithium-rich cathode ($\text{Li}_{1.2}\text{Mn}_{0.6}\text{Ni}_{0.2}\text{O}_2$) coated with a 4 V $\text{Li}_{1+x}\text{Mn}_2\text{O}_4$ spinel membrane for high-energy and high-power Li-ion batteries. The modified cathode displayed significant enhancements in specific capacity and cycling ability compared to an unmodified cathode. It yielded a maximal capacity of 295.6 mAh g^{-1} , and a capacity of 280.0 mAh g^{-1} by the 50th cycle, presenting excellent capacity retention at 94.7%. Yu et al. [40] reported an effective approach for synthesizing layered spinel-capped, nanotube-assembled 3D Li-rich architectures. The resulting material's unique 3D hollow hierarchical structure significantly shortened electron and ion transfer pathways whilst maintaining reliable structural stability. As a result, the $\text{LiMn}_{1.5}\text{Ni}_{0.5}\text{O}_4/\text{Li}_2\text{MnO}_3\text{-LiMn}_{0.4}\text{Ni}_{0.4}\text{Co}_{0.2}\text{O}_2$ composite components delivered a high capacity of 293 mAh g^{-1} at 0.1 C, showing strong capacity retention of 89.5% after 200 cycles at 1 C, and exhibited a high capacity of 202 mAh g^{-1} even at 5 C. To date, there have been few reports on the combined merits of layered and spinel materials to render a superior material in terms of kinetics, energetics, and stability [41–43]. Yin et al. [44] synthesized the high-voltage cathode of $\text{Li}_{1.2}\text{Mn}_{0.54}\text{Ni}_{0.13}\text{Co}_{0.13}\text{O}_2$ spheres coated with thin $\text{LiNi}_{0.5}\text{Mn}_{1.5}\text{O}_4$ layers via a simple coprecipitation method. This coated composite cathode recorded a superior rate capacity and stable cycle performance in the 2.0–4.8 V range. The $\text{Li}_{1.2}\text{Mn}_{0.54}\text{Ni}_{0.13}\text{Co}_{0.13}\text{O}_2/\text{LiNi}_{0.5}\text{Mn}_{1.5}\text{O}_4$ microsphere cathodes delivered a high capacity of 249.5 and 96 mAh g^{-1} at the rate of 0.2 C and 5 C, respectively. In addition, $\text{LiMn}_2\text{O}_4/\text{LiNi}_{0.5}\text{Mn}_{1.5}\text{O}_4$ hollow microspheres have been developed by Liu et al. [45], with a facile solution-phase coating and subsequent solid-phase lithiation route in an atmosphere of air. Their double-shell $\text{LiMn}_2\text{O}_4/\text{LiNi}_{0.5}\text{Mn}_{1.5}\text{O}_4$ hollow microspheres showed a high specific capacity of 120 mAh g^{-1} at a 1 C rate and an excellent rate capability (90 mAh g^{-1} at 10 C) over the 3.5–5 V range compared to Li/Li+, with a retention of 95% over 500 cycles.

In this experiment, a nanolayer of spinel LiCoMnO_4 (LCMO) was used as a coating because of its voltage stability window (5.3 V vs Li/Li+) [46–48]. In this composition, lithium-rich oxide contributes to high energy density, while the spinel nanolayer of LCMO provides structural stability to maintain the surface of the layered lithium-rich cathode during high-voltage cycling. Most importantly, this high Li^+ conductive nanolayer can rapidly transport Li^+ between the electrolyte and the layered lithium-rich cathode. Owing

to the high capacitance advantage of the lithium-rich cathode combined with the structural stability of the high-voltage spinel LCMO nanolayer, the electrochemical performance of lithium-rich cathode materials is expected to improve.

2. Materials and Methods

2.1. Cathode Preparation

The synthesis of $\text{Li}_{7/6}\text{Mn}_{1/2}\text{Ni}_{1/6}\text{Co}_{1/6}\text{O}_2$ was carried out via the coprecipitation of the precursor, $\text{Mn}_{1/2}\text{Ni}_{1/6}\text{Co}_{1/6}(\text{CO}_3)_{5/6}$. A 2 M solution of $\text{CoSO}_4 \cdot 7\text{H}_2\text{O}$, $\text{NiSO}_4 \cdot 7\text{H}_2\text{O}$, and $\text{MnSO}_4 \cdot \text{H}_2\text{O}$ was dropped into a continuous stirred-tank reactor. A 2 M Na_2CO_3 solution and an appropriate volume of NH_4OH solution as the chelating agent were then separately pumped into the reactor. The solutions were maintained at 60 °C, with a stirring speed of 1200 rpm and a pH of 8. After the reaction, the $\text{Mn}_{1/2}\text{Ni}_{1/6}\text{Co}_{1/6}(\text{CO}_3)_{5/6}$ precursor was filtered and air-dried.

The $\text{Mn}_{1/2}\text{Ni}_{1/6}\text{Co}_{1/6}(\text{CO}_3)_{5/6}$ precursor was added to the batch reactor as a core, and 1%, 2.5%, and 5% concentrations of $\text{CoSO}_4 \cdot 7\text{H}_2\text{O}$ and $\text{MnSO}_4 \cdot \text{H}_2\text{O}$ solutions at a molar ratio of $\text{Co}^{2+}:\text{Mn}^{2+} = 1:1$ were pumped in. A stoichiometric volume of Na_2CO_3 and an appropriate volume of NH_4OH were also added. After stirring for 12 h, the precursors of $\text{Mn}_{1/2}\text{Ni}_{1/6}\text{Co}_{1/6}(\text{CO}_3)_{5/6}$ coated with 0%, 1%, 2.5%, and 5% $\text{CoMn}(\text{CO}_3)_2$ were obtained. After drying, the coated precursors with 5% excess LiOH were calcined for 14 h at 900 °C to obtain $\text{Li}_{7/6}\text{Mn}_{1/2}\text{Ni}_{1/6}\text{Co}_{1/6}\text{O}_2$ cathodes coated with 0% (LR-Bare), 1% (LR-Sp1), 2.5% (LR-Sp2.5), and 5% (LR-Sp5) LiCoMnO_4 , respectively.

2.2. Characterization

Powder X-ray diffraction (XRD) measurements of the synthesized samples were performed using an X-ray diffractometer (D8A25, Bruker, USA) operated at 40 keV and 40 mA, using $\text{Cu K}\alpha$ radiation. Microstructural investigation of the powders was performed via a scanning electron microscopy (SEM, JSM-7500F, JEOL, Japan) and a high-resolution transmission electron microscope (HR-TEM, JEM-2100Plus JEOL, Japan). The particle sizes of the powders were measured using a static light-scattering analyzer (Mastersizer 2000, Malvern Instruments Ltd., UK), resulting in a measurement range of 0.04–2000 μm . The density of the cathode was measured using gas pycnometry (AccuPyc II, ATA scientific pty ltd, Australia), a non-destructive technique that employs gas displacement, often helium, to measure the volume of a material. The local structure of the sample was studied by Raman spectroscopy (MRI) using a laser with a wavelength of 532 nm and a power of 100 mW. Chemical state and composition analyses were then performed by X-ray photoelectron spectroscopy (XPS) using a Physical Electronics instrument (PHI 5000 VersaProbe III, ULVAC-PHI, Inc., Japan) with an Al X-ray source.

2.3. Electrochemical Measurements

The electrochemical properties were examined using a coin cell (CR-2032) with Li foil as the anode. Cathode electrodes were prepared by mixing 80 wt% as-prepared cathodes, 10 wt% acetylene carbon black, and 10 wt% polyvinylidene difluoride (PVDF) in an *n*-methyl-2-pyrrolidone solution. Next, the slurries were coated onto aluminum foil. The thickness of the loaded active materials was $31.6 \pm 4.2 \mu\text{m}$, whilst the mass loading was $7.9 \pm 0.2 \text{ mg cm}^{-2}$. An organic solution of 1 M LiPF_6 in ethylene carbonate (EC) and dimethyl carbonate (DMC) with a 1:2 volume ratio was used as the electrolyte. The charge-discharge profiles were measured at a current density of 20 mA g^{-1} (0.1 C) in the 2–4.8 V range for the formation process and then continually tested from a current density of 20 mA g^{-1} (0.1 C) to 1000 mA g^{-1} (5 C) within the 2–4.6 V range. After one formation cycle, the cycle life was determined by charging at 0.2 C and subsequent discharging at 0.5 C from 2 to 4.6 V. A second cycle life test was conducted at a high voltage of 4.9 V, with the same current density. The electrochemical impedance spectroscopy (EIS) test of the cells in reference to the Li/Li^+ couple was measured after 25 charge-discharge cycles at 2–4.6 V

and then again at a charged state of 4.2 V, within a frequency range of 0.01–100,000 Hz with a perturbation amplitude of 10 mV.

3. Results

3.1. Morphological Characterization

The surfaces and morphologies of the precursors were examined using electron microscopy, as shown in Figure 1. For the LR-Bare precursors, the nucleating cores of MCO_3 ($\text{M} = \text{Mn, Ni, Co}$) grew to form spherical primary particles with a diameter of 30 nm, as shown in Figure 1b. During the coprecipitation process, the primary particles aggregated into micro secondary particles with a spherical shape, as shown in Figure 1a, having the most stable thermodynamic state and minimal surface energy [49]. The primary particles of LR-Sp1 precursors with 1% nanolayer coverage had a size of 50–70 nm. When the coating concentration increased to 2.5%, the surface of the precursors was covered with dense square grains and a few flake particles. After a further increase to 5% coating, the flake particles on the surface of the precursors became larger.

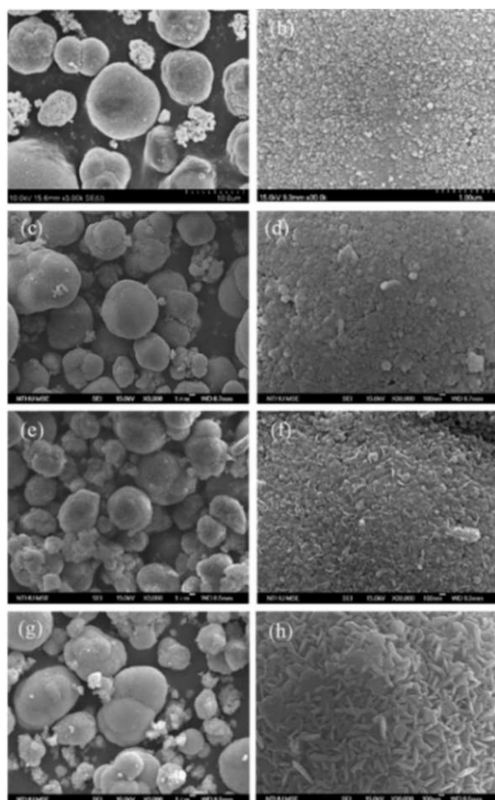


Figure 1. SEM images of (a,b) LR-Bare, (c,d) LR-Sp1, (e,f) LR-Sp2.5, and (g,h) LR-Sp5 precursors.

The precursors were calcined with the required amount of LiOH at 900 °C to form LR-Bare, LR-Sp1, LR-Sp2.5, and LR-Sp5 cathodes, and their morphologies are shown in Figure 2. The spherical primary particles of the LR-Bare cathode grew to 100 nm, whilst the primary particles of LR-Sp1, LR-Sp2.5, and LR-Sp5 also became spherical, with size growing alongside the increasing concentration, to eventually reach a diameter of approximately 200–300 nm. The secondary particle morphologies of all cathodes presented microspheres aggregation, and their mass median diameters (D_{50}) and true densities increased with the coating concentration. The mass median diameters (D_{50}) of secondary particles for LR-Bare, LR-Sp1, LR-Sp2.5, and LR-Sp5 cathodes were 7.2, 7.8, 8.6, and 8.9 μm , respectively, as shown in Figure 3. Meanwhile, the true densities of these cathodes were 4.02, 4.12, 4.18, and 4.28 g cm^{-3} , respectively.

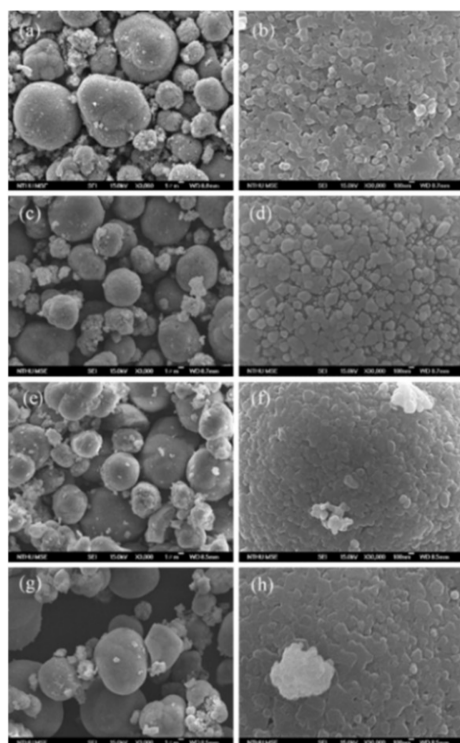


Figure 2. SEM images of (a,b) LR-Bare, (c,d) LR-Sp1, (e,f) LR-Sp2.5, and (g,h) LR-Sp5 cathodes.

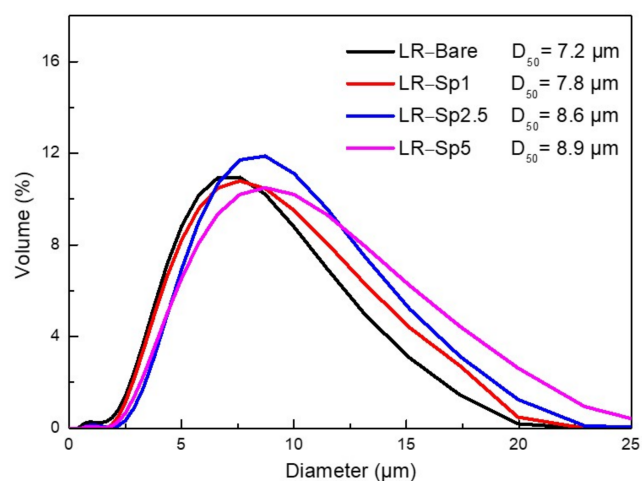


Figure 3. Size distribution of each cathode.

3.2. Structural Characterization

The structural characterization XRD patterns for all samples are plotted in Figure 4. The main peaks in the diffraction patterns of LR-Bare, LR-Sp1, LR-Sp2.5, and LR-Sp5 could be identified as that for hexagonal α - NaFeO_2 , with the space group of $R\bar{3}m$. On the other hand, the low-intensity superlattice peaks in the 2θ range of 20 – 25° could be attributed to the Li_2MnO_3 -like component, with a space group of $C2/m$ and the ordering of Li, Ni, and Mn atoms in the transition metal layers [50,51]. In the coated samples, the spinel structure of LiCoMnO_4 (LCMO) was not identified because of the cubic close-packing structures. This presented similar peaks with the XRD patterns of layered and spinel lithium metal oxides, making it difficult to distinguish the layered and spinel components from coated samples with low spinel content.

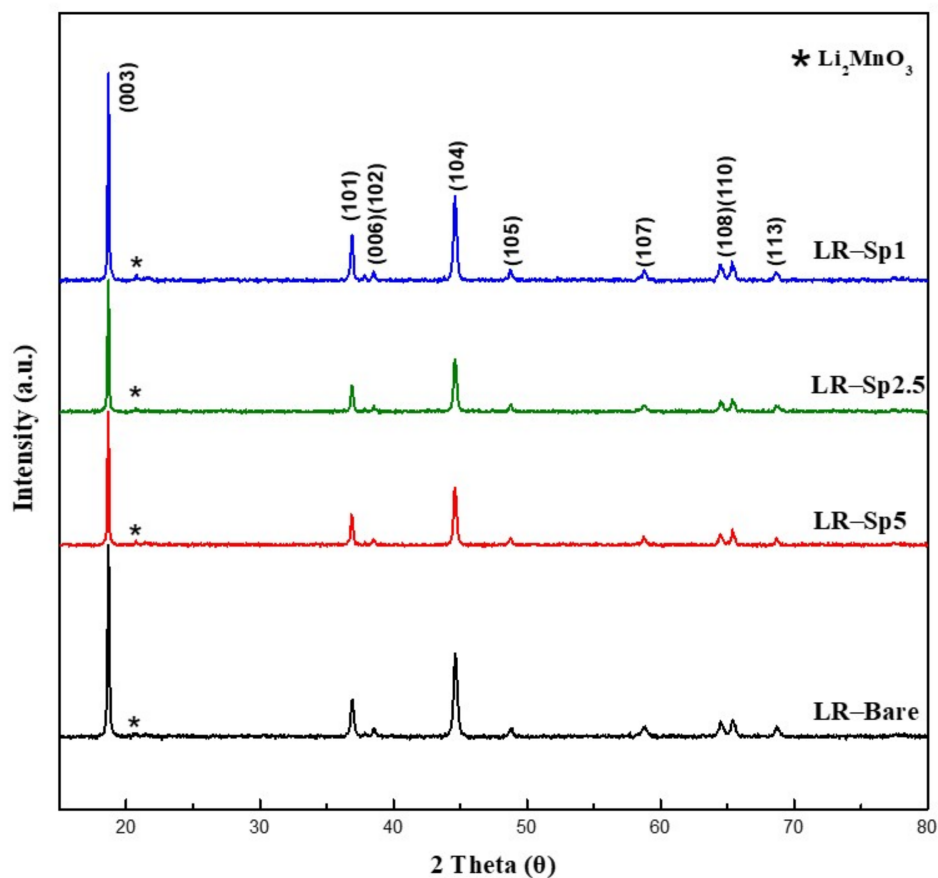


Figure 4. X-ray diffraction (XRD) patterns of the LR-Bare, LR-Sp1, LR-Sp2.5, and LR-Sp5 cathodes.

To further discern these spinel and layered structures, Raman spectroscopy was used to determine the short-range local structures of the materials. Figure 5 displays the Raman spectra of the four samples. The Raman bands located at 590, 471, and 425 cm^{-1} were observed in all samples, presenting typical characteristics of layered lithium-rich oxides, indicating that the layered structure was maintained after the deposition of the spinel nanolayer coating. There were two vibrational modes for the lithium-rich oxides with hexagonal $R\bar{3}m$ symmetry: E_g with symmetrical deformation and A_{1g} with the symmetrical stretching of M–O (M = Mn, Ni, and Co) [52]. The weak band at 425 cm^{-1} was the characteristic vibration of Li_2MnO_3 , which has monoclinic $C2/m$ symmetry and a lower local symmetry than $R\bar{3}m$ [40]. Meanwhile, two additional shoulder bands at around 635 and 551 cm^{-1} and another peak at 481 cm^{-1} in LR-Sp1, LR-Sp2.5, and LR-Sp5, as indicated by the blue arrows, were typical peaks of the spinel-phase with $Fd\bar{3}m$ symmetry [53,54]. Overall, the Raman spectra presented mixed characteristics of the spinel and layered phases for the coated samples.

To investigate the surface chemical states of the samples, X-ray photoelectron spectroscopy (XPS) measurements were obtained, as shown in Figure 6. The Ni 2p_{3/2} peaks at 854.5 and 860.9 eV indicated the coexistence of Ni²⁺ and Ni³⁺, as shown in Figure 6a [55]. In addition, the binding energy of 779.9 eV for the Co 2p_{3/2} peak was assigned to the Co³⁺ species, shown in Figure 6b [56]. Figure 6c shows that Mn p_{3/2} and Mn 2p_{1/2} had binding energies of 641.9 and 653.2 eV, respectively, which are typical values for Mn⁴⁺ [57,58]. The Mn, Ni, and Co XPS peaks for LR-Bare and LR-Sp2.5 presented the same binding energies. Figure 6d compares the O 1s peaks; there were two pronounced peaks at 528.9 and 530.6 eV, which corresponded to lattice oxygen atoms (O–M–O) and oxygen vacancies, respectively. The O 1s peak areas of LR-Sp2.5, especially the peak of oxygen vacancies, were smaller than those for LR-Bare, which indicated that the LCMO spinel nanolayer was

successfully constructed on the surface of the layered lithium-rich oxides, thus exhibiting good structural compatibility.

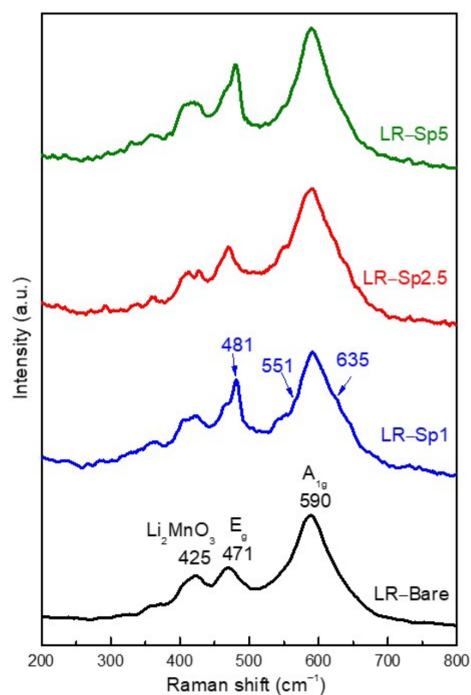


Figure 5. Raman spectra of the LR-Bare, LR-Sp1, LR-Sp2.5, and LR-Sp5 cathodes.

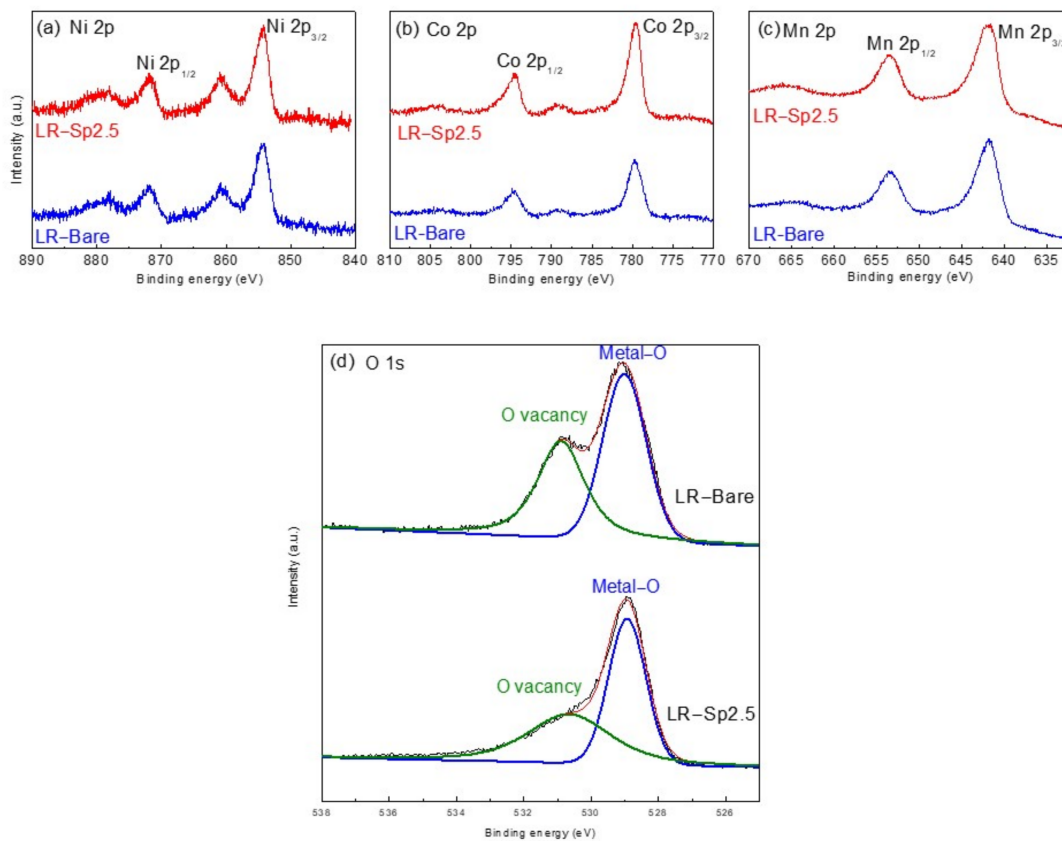


Figure 6. XPS spectra of (a) Ni 2p, (b) Co 2p, (c) Mn 2p, and (d) O 1s for LR-Bare and LR-Sp2.5 cathodes.

3.3. Electrochemical Characterization

The charge–discharge rate performances of the samples at 0.1 C over 2.0–4.8 V during the formation process and at 0.1, 1, and 5 C between 2.0 and 4.6 V are presented in Figure 7. LR-Bare had the lowest rate capability, alongside a dramatic capacity drop with an increase in C-rate; this was because of the fast Li^+ insertion and extraction, which damaged the fragile surface of the layered structure at a high rate. The C-rate results for LR-Sp1 were similar to those for LR-Bare because of the low concentration of the spinel nanolayer. LR-Sp2.5 and LR-Sp5, especially the former, exhibited superior discharge capacities and C-rate performances compared to LR-Bare. These results indicate that the Li-rich layered oxide with LCMO spinel nanolayer provided the combined advantages of high capacity from the Li-rich layered oxide and high rate capability from the spinel nanolayer. The discharge capacities of LR-Bare were 271, 254, 193, and 144 mAh g^{-1} at 0.1 C and 2.0–4.8 V during formation and at rates of 0.1, 1, and 5 C across 2.0–4.6 V, respectively. Under the same conditions, LR-Sp2.5 exhibited excellent discharge capacities of 300, 275, 220, and 166 mAh g^{-1} , respectively. Thus, it is believed that an optimal concentration of the LCMO spinel nanolayer has good structural compatibility with Li-rich layered oxides and can provide relatively high working C-rates owing to 3D interstitial spaces [59]; this accelerates lithium-ion insertion and extraction kinetics [60,61].

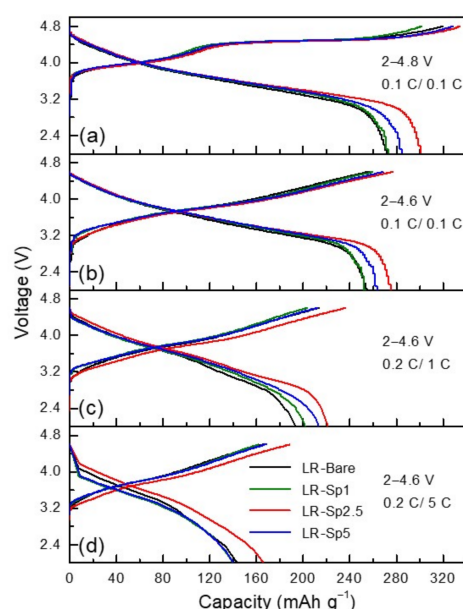


Figure 7. Charge and discharge performance at (a) 0.1 C/0.1 C between 2–4.8 V, (b) 0.1 C/0.1 C, (c) 0.2 C/1 C and (d) 0.2 C/5 C between 2–4.6 V for the LR-Bare, LR-Sp1, LR-Sp2.5, and LR-Sp5 cathodes.

After formation at 2.0–4.8 V, the cycle performance of the samples was tested for 100 cycles at 0.2 C/0.5 C charge–discharge between 2.0 and 4.6 V, with these results shown in Figure 8. When cycling for 60 cycles, the capacities of all samples were stable at approximately 200 mAh g^{-1} ; however, after 60 cycles, the capacity of LR-Bare began to decrease rapidly. After 100 cycles, the discharge capacity of LR-Bare was 150.5 mAh g^{-1} . In contrast, remarkably improved cycling stability was observed in the samples with the LCMO spinel nanolayers. Even after 100 cycles, the discharge capacities of LR-Sp1, LR-Sp2.5, and LR-Sp5 remained at 183.7, 193.6, and 192.1 mAh g^{-1} , respectively. This is because the spinel nanolayer prevented phase transition on the Li-rich layered oxide surface during cycling, thus improving the cycle performance. Therefore, it prevented the generation of stress induced by the anisotropic volume change of the primary crystallites in secondary particles, further preventing the generation of cracks [58]. Overall, samples with spinel nanolayers displayed better cycle performance [62].

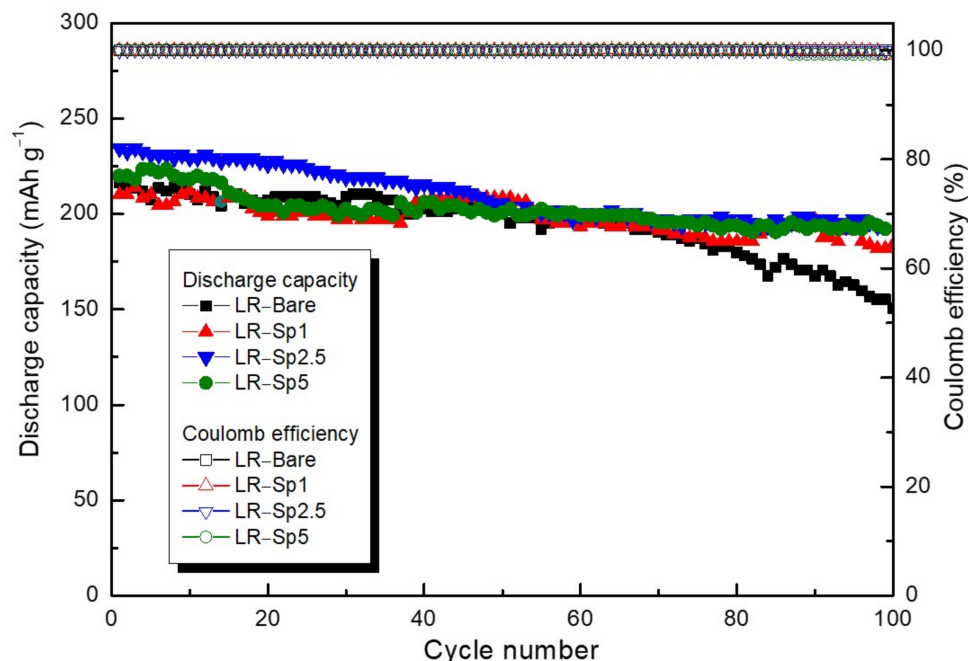


Figure 8. Cycle life performance of LR-Bare, LR-Sp1, LR-Sp2.5, and LR-Sp5 cathodes at 2–4.6 V.

To explain the electrochemical properties of LR-Bare and LR-Sp2.5, electrochemical impedance spectroscopy (EIS) was operated after 25 charge–discharge cycles at 2.0–4.6 V and then in a charged state at 4.2 V. The impedance spectra shown in Figure 9 contained the bulk resistance of the electrolyte (R_e), the resistance at the contact of the composite cathode (R_{SEI}), the charge transfer resistance at the interface of the cathode–electrolyte (R_{ct}), and a line inclined at a constant angle to the real axis in the low–frequency range corresponding to Li^+ diffusion in the materials [5,55,58]. The R_{ct} and lithium ion diffusion coefficient (D_{Li^+}) were 23.1Ω and $2.96 \times 10^{-12} \text{ cm}^2 \text{ s}^{-1}$ for LR-Bare and 20.0Ω and $3.21 \times 10^{-12} \text{ cm}^2 \text{ s}^{-1}$ for LR-Sp2.5, respectively. This shows that the sample with a spinel nanolayer had the fastest lithium–ion insertion and extraction kinetics at the electrolyte–electrolyte interface.

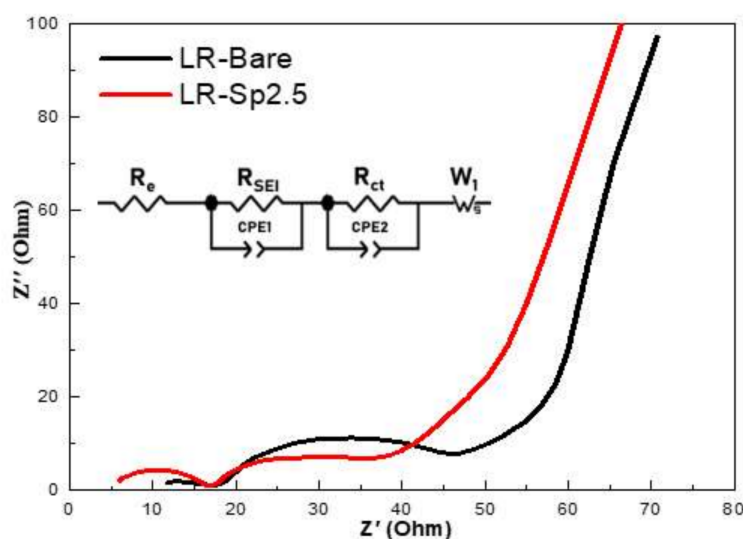


Figure 9. Electrochemical impedance spectra of LR-Bare and LR-Sp2.5 after 25 charge–discharge cycles.

Transmission electron microscopy (TEM) was further utilized to study the detailed morphological structures of LR-Bare and LR-Sp2.5 samples. LR-Bare is an agglomerated

secondary particle with nanosized primary grains, as shown in Figure 10a. In Figure 10b, LR-Bare presents a smooth edge line without any other layer on the surface of the grain. During long-term cycling, partial cation ordering in the layered structure of LR-Bare was locally rearranged into an inactive phase that contained transition metal ions in both the lithium and transition metal layers [63]. The phase transformation accompanied the lattice strain in the grains; consequently, nanosized domains were identified in LR-Bare grains, which developed into a polycrystalline structure after 100 cycles, as shown in Figure 10c,d. After modification with the LCMO spinel nanolayer, LR-Sp2.5 was covered by a thin film with a width of 5–8 nm, as shown in Figure 10e. Throughout 100 cycles, LR-Sp2.5 exhibited polycrystalline and intact grains, as shown in Figure 10f,g. According to Gu [64] and Xu et al. [12], the migration of transition metal ions to Li layers leads to a layered-to-inactive spinel phase transformation, which only occurs at the surface of the particles in the beginning. During long-term cycling, the inactive spinel phase transformation extends to the inner parts of the particles. In our study, after 100 cycles, LR-Sp2.5 presented mosaic grains coated with a spinel nanolayer (Figure 10f) and undamaged particles without a coating (Figure 10g). Therefore, we presume the former was likely located on the outer surface, and the latter was present in the center of the microsphere aggregates of the LR-Sp2.5 particle. This proves that the LCMO spinel nanolayer could effectively stabilize the structure and relieve the particle damage caused by phase transformation, thereby protecting the inner particles, and allowing them to function normally.

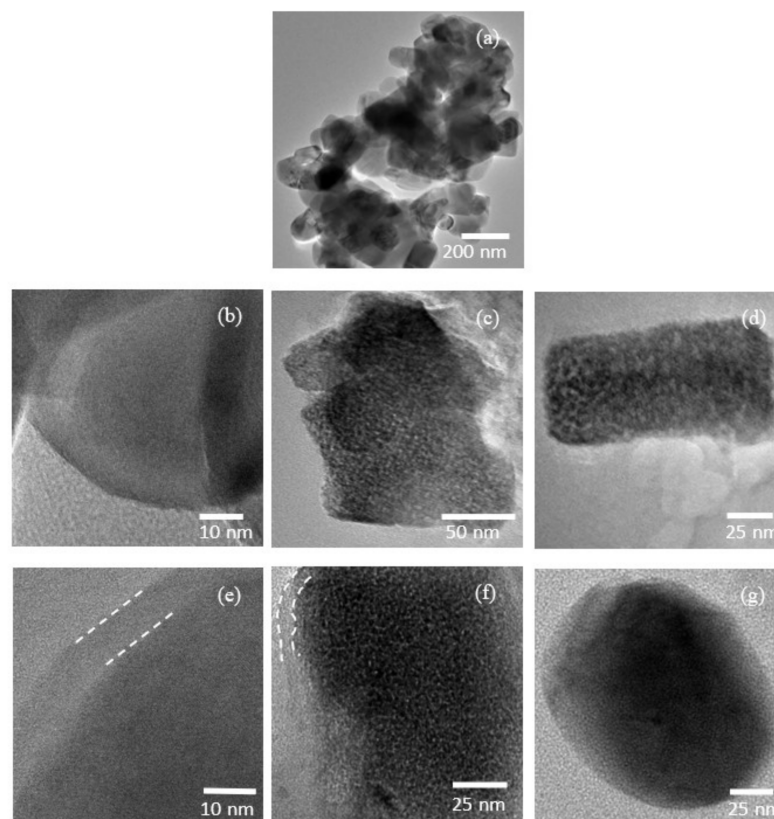


Figure 10. Transmission electron microscopy (TEM) images of (a,b) LR-Bare before cycle and (c,d) after 100 cycles; and (e) LR-Sp2.5 before cycle and (f,g) after 100 cycles.

To further understand the utility of the LCMO spinel nanolayer under high voltage on the Li-rich layered oxide, the range of the charge–discharge voltage was raised to 2.0–4.9 V. The cycle performances of the samples at 0.2 C and 0.5 C and charge–discharge at 4.9 V are shown in Figure 11a. In this case, the capacity of LR-Bare decayed very quickly with an increasing number of cycles owing to the high voltage, and the battery completely

failed after 42 cycles. On the contrary, the samples with the LCMO spinel nanolayers showed better cycling performance, with LR–Sp2.5 having the best and most stable capacity retention. Figure 11b–e shows the discharge profiles of LR–Bare, LR–Sp1, LR–Sp2.5, and LR–Sp5 for cycles 10, 20, 30, and 40, respectively. In Figure 11b, LR–Bare delivered a capacity of 228.5 mAh g^{−1} at the 10th cycle, but a capacity of only 28.1 mAh g^{−1} remained after 40 cycles, alongside significant voltage fading. For LR–Sp1 and LR–Sp5 in Figure 11c,e, the capacity was approximately 230 mAh g^{−1} at the 10th cycle. However, capacity and voltage had rapidly decayed by the 20th cycle before stabilizing during later cycles. However, LR–Sp1 completely failed after 45 cycles because of the low concentration of the LCMO spinel nanolayer. In Figure 11d, LR–Sp2.5 demonstrated significant improvements in both specific capacity and voltage maintenance with increasing cycles at 2.0–4.9 V. LCMO is a high–voltage cathode material with an operating voltage of approximately 5.3 V [48]; therefore, its electrochemical performance is stable at 4.9 V. When LCMO is used as a coating layer, it can yield good structural compatibility to stabilize the surface of the Li–rich layered oxide and avoid the generation of oxygen vacancies, which is induced by the phase transformation from the layered structure to the inactive spinel structure at the surface. In addition, LCMO can suppress the side reactions caused by the electrolyte at high voltages. These features enhance the diffusion kinetics of Li ions, improve cycling performance, and alleviate voltage decay.

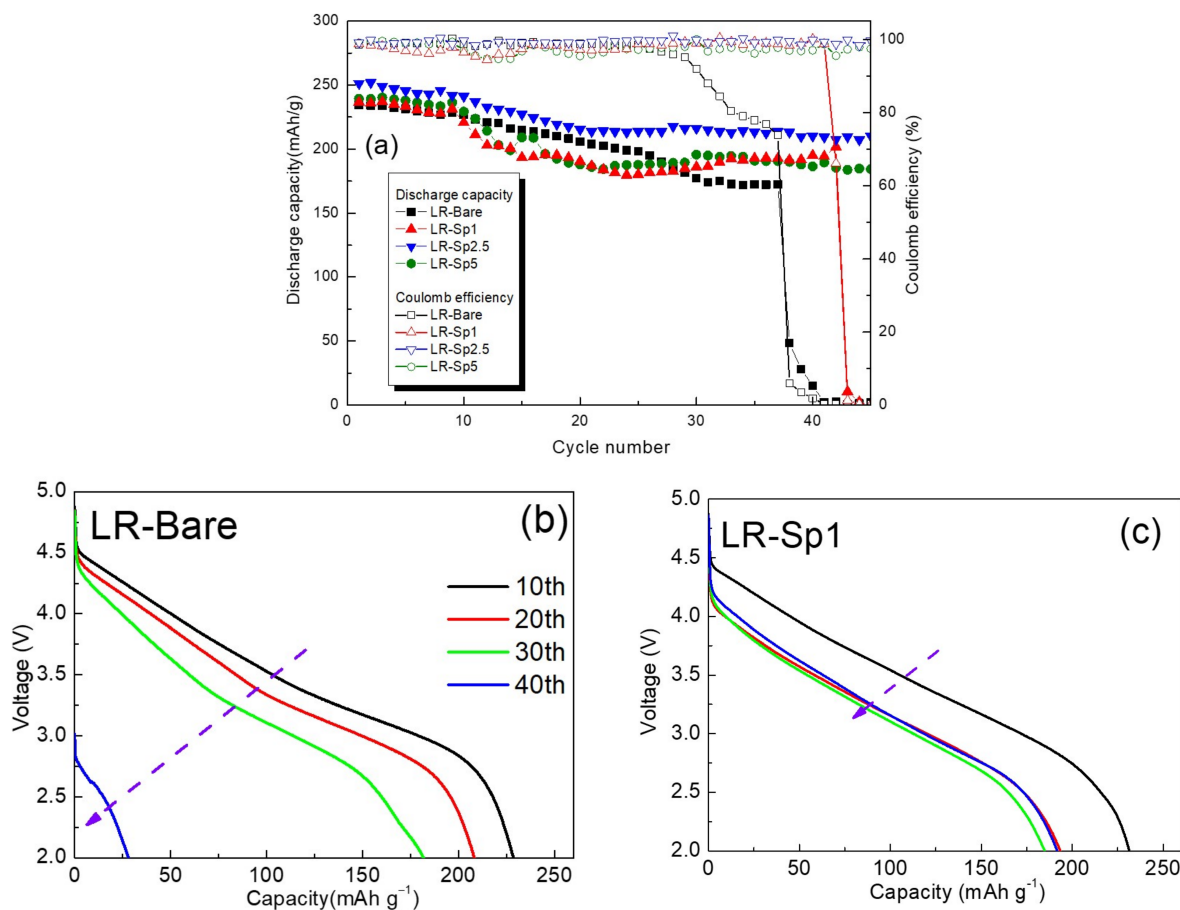


Figure 11. Cont.

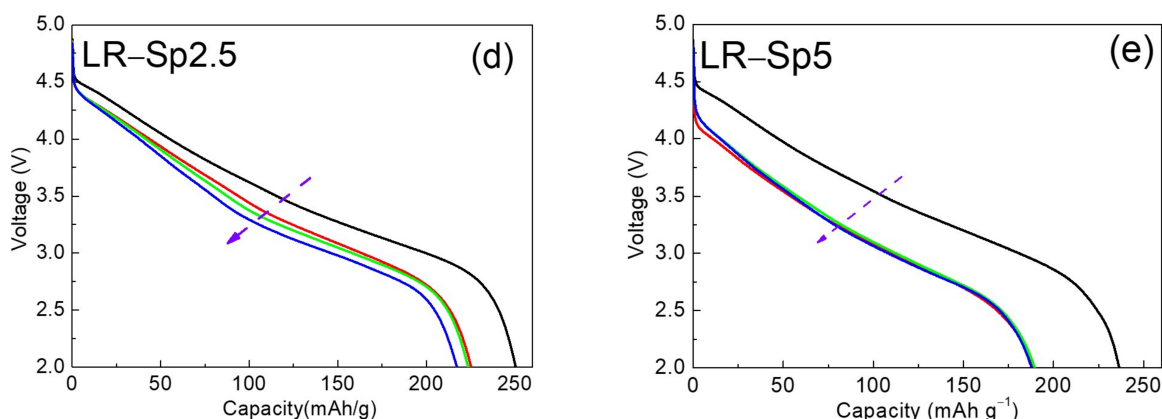


Figure 11. (a) Cycle life performance and discharge profiles for the 10th, 20th, 30th, and 40th cycles for (b) LR-Bare, (c) LR-Sp1, (d) LR-Sp2.5, and (e) LR-Sp5 cathodes at 2.0–4.9 V.

The differential capacity vs. voltage (dQ/dV) curves provide a clear perspective on the electrochemical reactions that occur during cycling. Figure 12 shows the dQ/dV curves of LR-Bare and LR-Sp2.5 cathodes cycled at 0.2 C and 0.5 C across 2.0–4.9 V. There were three redox reactions corresponding to Mn, Ni, Co, and O. For LR-Bare, two anodic peaks of $Mn^{3+/4+}$ were observed; the first one, at 3.1 V, was induced by Mn in an inactive spinel structure and the other one, at 3.3 V, was related to Mn in the Li-rich layered oxides [65,66]. A prominent oxygen-activating peak also appeared at approximately 4.5 V, which was related to the layered-to-inactive spinel phase transformation of Li-rich layered oxides [67–70], as shown in Figure 12a. In Figure 12b, the divided peak of Mn was not observed, and the intensity of the O^{2-} anodic peak for LR-Sp2.5 was much lower than those of LR-Bare. In addition, during the cycling, LR-Sp2.5 presented greater overlap among the cathodic peaks of Mn compared with LR-Bare. This indicates that LR-Sp2.5 exhibited inconspicuous polarization at a higher cutoff voltage of 4.9 V than LR-Bare. After cycling at high voltage, the LCMO spinel nanolayer maintained the structural stability of the lithium-rich oxide surface, thereby suppressing phase transformation and crystallographic distortions.

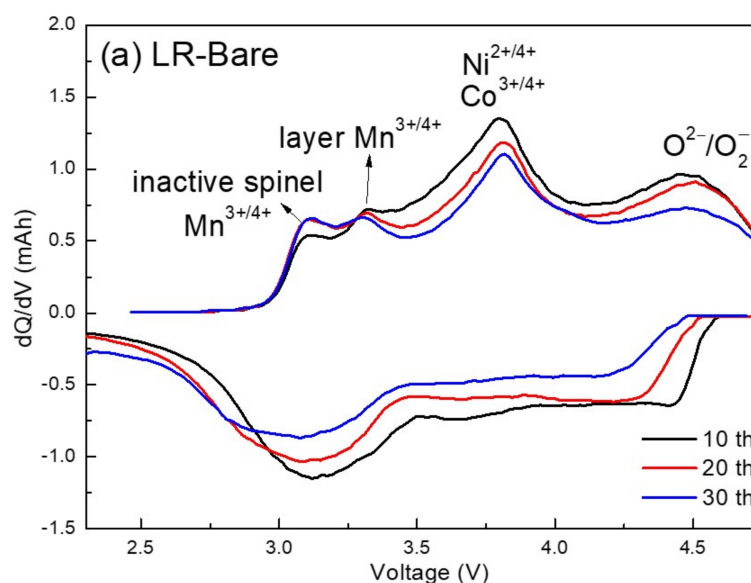


Figure 12. Cont.

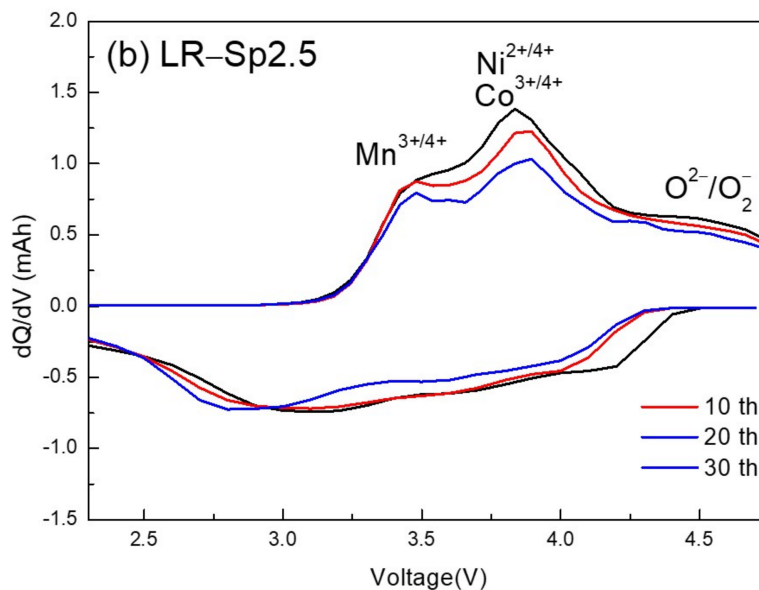


Figure 12. Differential capacity curves of (a) LR-Bare and (b) LR-Sp2.5 cathodes for the 10th, 20th, and 30th cycles.

4. Conclusions

Lithium-rich oxides, $\text{Li}_{7/6}\text{Mn}_{1/2}\text{Ni}_{1/6}\text{Co}_{1/6}\text{O}_2$, were successfully modified with a LiCoMnO_4 (LCMO) spinel nanolayer on the surface using a coprecipitation method. The LCMO spinel nanolayer effectively prevented side reactions between the lithium-rich oxide and organic electrolytes, thereby promoting ion and charge transfer on the surface of the lithium-rich oxides. Meanwhile, the LCMO nanolayer could effectively restrain the migration of transition metal ions and the generation of oxygen vacancies induced by the phase transformation from the layered structure to the inactive spinel structure at the surface of lithium-rich oxides. As a result, the obtained LR-Sp2.5 showed excellent cycle and rate performances during cycling at normal (4.6 V) and high (4.9 V) voltages.

Author Contributions: H.-F.L.: Conceptualization, Methodology, Validation, Data curation, Writing—original draft, Formal analysis, Writing—review & editing, Visualization, Supervision, Project administration. S.-T.C.: Investigation, Formal analysis, Data curation, Formal analysis, Project administration. D.-Z.C.: Investigation, Formal analysis. N.-Y.W.: Investigation, Formal analysis. Z.-X.J.: Data curation. C.-T.C.: Data curation. All authors have read and agreed to the published version of the manuscript.

Funding: This study was supported by the Ministry of Science and Technology of the Republic of China (MOST 110-2637-E-150-010 and MOST 110-3116-F-011-002).

Acknowledgments: The authors appreciate the technical support from the Industrial Technology Research Institute and Common Laboratory for Micro/Nano Science and Technology of National Formosa University.

Conflicts of Interest: The authors declare no conflict of interest.

References

- Goodenough, J.B.; Park, K. -S. The Li-ion rechargeable battery: A perspective. *J. Am. Chem. Soc.* **2013**, *135*, 1167–1176. [[CrossRef](#)] [[PubMed](#)]
- Thackeray, M.M.; Wolverton, C.; Isaacs, E.D. Electrical energy storage for transportation—approaching the limits of, and going beyond, lithium-ion batteries. *Energy Environ. Sci.* **2012**, *5*, 7854–7863. [[CrossRef](#)]
- Yu, R.; Wang, X.; Fu, Y.; Wang, L.; Cai, S. Effect of magnesium doping on properties of lithium-rich layered oxide cathodes based on a one-step co-precipitation strategy. *J. Mater. Chem. A* **2016**, *4*, 4941–4951. [[CrossRef](#)]
- Pang, W.K.; Lin, H.-F.; Peterson, V.K.; Lu, C.-Z.; Liu, C.-E.; Liao, S.-C.; Chen, J.M. Effects of Fluorine and Chromium Doping on the Performance of Lithium-Rich $\text{Li}_{1+x}\text{MO}_2$ (M = Ni, Mn, Co) Positive Electrode. *Chem. Mater.* **2017**, *29*, 10299–10311. [[CrossRef](#)]

5. Lin, H.-F.; Guo, H.-L.; Hsiao, S.-C. Electrochemical performances of lithium rich cathodes prepared via co-precipitation method with different precipitator and atmosphere. *J. Mater. Sci. Mater. Electron.* **2018**, *29*, 10427–10436. [[CrossRef](#)]
6. Yang, X.; Wang, D.; Yu, R.; Bai, Y.; Shu, H.; Ge, L.; Guo, H.; Wei, Q.; Liu, L.; Wang, X. Suppressed capacity/voltage fading of high-capacity lithium-rich layered materials via the design of heterogeneous distribution in the composition. *J. Mater. Chem. A* **2014**, *2*, 3899–3911. [[CrossRef](#)]
7. Wang, G.; Wang, X.; Yi, L.; Yu, R.; Liu, M.; Yang, X. Preparation and performance of $0.5\text{Li}_2\text{MnO}_3 \cdot 0.5\text{LiNi}_{1/3}\text{Co}_{1/3}\text{Mn}_{1/3}\text{O}_2$ with a fusiform porous micro-nano structure. *J. Mater. Chem. A* **2016**, *4*, 15929–15939. [[CrossRef](#)]
8. Li, J.; Camardese, J.; Glazier, S.; Dahn, J.R. Structural and Electrochemical Study of the Li-Mn-Ni Oxide System within the Layered Single Phase Region. *Chem. Mater.* **2014**, *26*, 7059–7066. [[CrossRef](#)]
9. Martha, S.K.; Nanda, J.; Veith, G.M.; Dudney, N.J. Electrochemical and rate performance study of high-voltage lithium-rich composition: $\text{Li}_{1.2}\text{Mn}_{0.525}\text{Ni}_{0.175}\text{Co}_{0.1}\text{O}_2$. *J. Power Source* **2012**, *199*, 220–226. [[CrossRef](#)]
10. Thackeray, M.M.; Kang, S.-H.; Johnson, C.S.; Vaughey, J.T.; Benedek, R.; Hackney, S.A. Li_2MnO_3 -stabilized LiMO_2 (M= Mn, Ni, Co) electrodes for lithium-ion batteries. *J. Mater. Chem.* **2007**, *17*, 3112. [[CrossRef](#)]
11. Wang, D.; Belharouak, I.; Zhou, G.K. Amine Nanoarchitecture Multi-Structural Cathode Materials for High Capacity Lithium Batteries. *Adv. Funct. Mater.* **2012**, *23*, 1070. [[CrossRef](#)]
12. Xu, B.; Fell, C.R.; Chi, M.; Meng, Y.S. Identifying surface structural changes in layered Li-excess nickel manganese oxides in high voltage lithium ion batteries: A joint experimental and theoretical study. *Energy Environ. Sci.* **2011**, *4*, 2223. [[CrossRef](#)]
13. Kottegoda, I.R.M.; Kadoma, Y.; Ikuta, H.; Uchimoto, Y.; Wakihara, M. Enhancement of Rate Capability in Graphite Anode by Surface Modification with Zirconia. *Electrochem. Solid State Lett.* **2002**, *5*, A275. [[CrossRef](#)]
14. Eftekhari, A. Surface Modification of Thin-Film Based LiCoPO_4 5 V Cathode with Metal Oxide. *J. Electrochem. Soc.* **2004**, *151*, A1456. [[CrossRef](#)]
15. Van Landschoot, N.; Kelder, E.M.; Kooyman, P.J.; Kwakernaak, C.; Schoonman, J. Electrochemical performance of Al_2O_3 -coated Fe doped LiCoVO_4 . *J. Power Source* **2004**, *138*, 262. [[CrossRef](#)]
16. Sun, Y.-K.; Yoon, C.S.; Oh, I.-H. Surface structural change of ZnO -coated $\text{LiNi}_0.5\text{Mn}_{1.5}\text{O}_4$ spinel as 5 V cathode materials at elevated temperatures. *Electrochim. Acta* **2002**, *48*, 503.
17. Miyashiro, H.; Yamanaka, A.; Tabuchi, M.; Seki, S.; Nakayama, M.; Ohno, Y.; Kobayashi, Y.; Mita, Y.; Usami, A.; Wakihara, M. Improvement of degradation at elevated temperature and at high state-of-charge storage by ZrO_2 coating on LiCoO_2 . *J. Electrochem. Soc.* **2006**, *153*, A348. [[CrossRef](#)]
18. Lin, Y.-M.; Wu, H.-C.; Yen, Y.-C.; Guo, Z.-Z.; Yang, M.-H.; Chen, H.-M.; Sheu, H.-S.; Wu, N.-L. Enhanced High-Rate Cycling Stability of LiMn_2O_4 Cathode by ZrO_2 Coating for Li-Ion Battery. *J. Electrochem. Soc.* **2005**, *152*, A1526. [[CrossRef](#)]
19. Zhao, T.; Li, L.; Chen, R.; Wu, H.; Zhang, X.; Chen, S.; Xie, M.; Wu, F.; Lu, J. Amine Design of surface protective layer of LiF/FeF_3 nanoparticles in Li-rich cathode for high-capacity Li-ion batteries. *Nano Energy* **2015**, *15*, 164–176. [[CrossRef](#)]
20. Zheng, J.; Gu, M.; Xiao, J.; Polzin, B.J.; Yan, P.; Chen, X.; Wang, C.; Zhang, G.-J. Functioning Mechanism of AlF_3 Coating on the Li- and Mn-Rich Cathode Materials. *Chem. Mater.* **2014**, *26*, 6320–6327. [[CrossRef](#)]
21. Xia, Q.; Zhao, X.; Xu, M.; Ding, Z.; Liu, J.; Chen, L.; Ivey, D.G.; Wei, W. A Li-rich Layered-Spinel-Carbon heterostructured cathode material for high capacity and high rate lithium-ion batteries fabricated via an in situ synchronous carbonization-reduction method. *J. Mater. Chem. A* **2015**, *3*, 3995–4003. [[CrossRef](#)]
22. Sun, Y.-K.; Lee, M.-J.; Yoon, C.S.; Hassoun, J.; Amine, K.; Scrosati, B. The Role of AlF_3 Coatings in Improving Electrochemical Cycling of Li-Enriched Nickel-Manganese Oxide Electrodes for Li-Ion Batteries. *Adv. Mater.* **2012**, *24*, 1192. [[CrossRef](#)] [[PubMed](#)]
23. Croy, J.R.; Balasubramanian, M.; Kim, D.; Kang, J.-S.; Thackeray, M.M. Designing High-Capacity, Lithium-Ion Cathodes Using X-ray Absorption Spectroscopy. *Chem. Mater.* **2011**, *23*, 5415. [[CrossRef](#)]
24. Zhang, X.; Sun, S.; Wu, Q.; Wan, N.; Pan, D.; Bai, Y. Improved electrochemical and thermal performances of layered $\text{Li}[\text{Li}_{0.2}\text{Ni}_{0.17}\text{Co}_{0.07}\text{Mn}_{0.56}]\text{O}_2$ via Li_2ZrO_3 surface modification. *J. Power Source* **2015**, *282*, 378–384. [[CrossRef](#)]
25. Liu, W.; Oh, P.; Liu, X.; Myeong, S.; Cho, W.; Cho, J. Countering Voltage Decay and Capacity Fading of Lithium-Rich Cathode Material at 60 °C by Hybrid Surface Protection Layers. *Adv. Energy Mater.* **2015**, *5*, 1500274. [[CrossRef](#)]
26. Lee, S.; Cho, Y.; Song, H.-K.; Lee, K.T.; Cho, J. Carbon-Coated Single-Crystal LiMn_2O_4 Nanoparticle Clusters as Cathode Material for High-Energy and High-Power Lithium-Ion Batteries. *Angew. Chem. Int. Ed.* **2012**, *51*, 8748–8752. [[CrossRef](#)]
27. Zhou, L.; Zhao, D.; Lou, X.W. $\text{LiNi}_{0.5}\text{Mn}_{1.5}\text{O}_4$ Hollow Structures as High-Performance Cathodes for Lithium-Ion Batteries. *Angew. Chem. Int. Ed.* **2012**, *51*, 239. [[CrossRef](#)]
28. Thackeray, M.M. Lithium-ion batteries: An unexpected conductor. *Nat. Mater.* **2002**, *1*, 81. [[CrossRef](#)]
29. Liao, C.; Li, F.; Liu, J. Challenges and Modification Strategies of Ni-Rich Cathode Materials Operating at High-Voltage. *Nanomaterials* **2022**, *12*, 1888. [[CrossRef](#)]
30. Su, Y.; Chen, G.; Chen, L.; Li, Q.; Lu, Y.; Bao, L.; Li, N.; Chen, S.; Wu, F. Advances and Prospects of Surface Modification on Nickel-Rich Materials for Lithium-Ion Batteries. *Chin. J. Chem.* **2019**, *37*, 1817–1831. [[CrossRef](#)]
31. Huang, Y.; Zhang, X.; Yu, R.; Jamil, S.; Cao, S.; Fang, S.; Wang, Y.; Tang, K.; Chen, G.; Luo, Z.; et al. Preparation and Performance of the Heterostructured Material with a Ni-Rich Layered Oxide Core and a $\text{LiNi}_{0.5}\text{Mn}_{1.5}\text{O}_4$ -like Spinel Shell. *ACS Appl. Mater. Inter.* **2019**, *11*, 16556–16566. [[CrossRef](#)] [[PubMed](#)]
32. Min, K.; Jung, C.; Ko, D.-S.; Kim, K.; Jang, J.; Park, K.; Cho, E. High-Performance and Industrially Feasible Ni-Rich Layered Cathode Materials by Integrating Coherent Interphase. *ACS Appl. Mater. Inter.* **2018**, *10*, 20599–20610. [[CrossRef](#)] [[PubMed](#)]

33. Zheng, Y.; Chen, L.; Su, Y.; Tan, J.; Bao, L.; Lu, Y.; Wang, J.; Chen, R.; Chen, S.; Wu, F. An interfacial framework for breaking through the Li-ion transport barrier of Li-rich layered cathode materials. *J. Mater. Chem. A* **2017**, *5*, 24292. [[CrossRef](#)]
34. Chen, S.; Zheng, Y.; Lu, Y.; Su, Y.; Bao, L.; Li, N.; Li, Y.; Wang, J.; Chen, R.; Wu, F. Enhanced Electrochemical Performance of Layered Lithium-Rich Cathode Materials by Constructing Spinel-Structure Skin and Ferric Oxide Islands. *Appl. Mater. Interfaces* **2017**, *9*, 8669–8678. [[CrossRef](#)] [[PubMed](#)]
35. Zhang, X.; Shi, J.; Liang, J.; Yin, Y.; Zhang, J.; Yu, X.; Guo, Y. Suppressing Surface Lattice Oxygen Release of Li-Rich Cathode Materials via Heterostructured Spinel $\text{Li}_4\text{Mn}_5\text{O}_{12}$ Coating. *Adv. Mater.* **2018**, *30*, 1801751. [[CrossRef](#)] [[PubMed](#)]
36. Park, K.; Yeon, D.; Kim, J.H.; Park, J.H.; Doo, S.; Choi, B. Spinel-embedded lithium-rich oxide composites for Li-ion batteries. *J. Power Source* **2017**, *360*, 453–459. [[CrossRef](#)]
37. Freitas, R.R.Q.; de Brito Mota, F.; Rivelino, R.; de Castilho, C.M.C.; Kakanakova-Georgieva, A.; Gueorguiev, G.K. Spin-orbit-induced gap modification in buckled honeycomb XBi and XBi₃ (X = B, Al, Ga, and In) sheets. *J. Phys. Condens. Matter* **2015**, *27*, 485306. [[CrossRef](#)]
38. Bakoglidis, K.D.; Palisaitis, J.; dos Santos, R.B.; Rivelino, R.; Persson, P.O.Å.; Gueorgui, K.; Gueorguiev Hultman, L. Self-Healing in Carbon Nitride Evidenced As Material Inflation and Superlubric Behavior. *ACS Appl. Mater. Interfaces* **2018**, *10*, 16238–16243. [[CrossRef](#)] [[PubMed](#)]
39. Wu, F.; Li, N.; Su, Y.; Zhang, L.; Bao, L.; Wang, J.; Chen, L.; Zheng, Y.; Dai, L.; Peng, J. Ultrathin Spinel Membrane-Encapsulated Layered Lithium-Rich Cathode Material for Advanced Li-Ion Batteries. *Nano Lett.* **2014**, *14*, 3550–3555.
40. Yu, F.-D.; Que, L.-F.; Wang, Z.-B.; Zhang, Y.; Xue, Y.; Liu, B.-S.; Gu, D.-M. Layered-spinel capped nanotube assembled 3D Li-rich architectures for high performance Li-ion battery cathodes. *Mater. Chem. A* **2016**, *4*, 18416. [[CrossRef](#)]
41. Cho, Y.; Lee, S.; Lee, Y.; Hong, T.; Cho, J. Spinel-Layered Core-Shell Cathode Materials for Li-Ion Batteries. *Adv. Energy Mater.* **2011**, *1*, 821. [[CrossRef](#)]
42. Park, S.-H.; Kang, S.-H.; Johnson, C.-S.; Amine, K.; Thackeray, M.M. Lithium-manganese-nickel-oxide electrodes with integrated layered-spinel structures for lithium batteries. *Electrochem. Commun.* **2007**, *9*, 262. [[CrossRef](#)]
43. Lee, E.-S.; Huq, A.; Chang, H.-Y.; Manthiram, A. High-Voltage, High-Energy Layered-Spinel Composite Cathodes with Superior Cycle Life for Lithium-Ion Batteries. *Chem. Mater.* **2012**, *24*, 600. [[CrossRef](#)]
44. Yin, H.; Ji, S.; Gu, M.; Zhang, L.; Liu, J. Scalable Synthesis of $\text{Li}_{1.2}\text{Mn}_{0.54}\text{Ni}_{0.13}\text{Co}_{0.13}\text{O}_2/\text{LiNi}_{0.5}\text{Mn}_{1.5}\text{O}_4$ Sphere Composites as Stable and High Capacity Cathode for Li-Ion. *RSC Adv.* **2015**, *5*, 84673–84679. [[CrossRef](#)]
45. Liu, W.; Liu, J.; Chen, K.; Ji, S.; Wan, Y.; Zhou, Y.; Xue, D.; Hodgson, P.; Li, Y. Enhancing the Electrochemical Performance of the LiMn_2O_4 Hollow Microsphere Cathode with a $\text{LiNi}_{0.5}\text{Mn}_{1.5}\text{O}_4$ Coated Layer. *Chem. Eur. J.* **2014**, *20*, 824–830. [[CrossRef](#)] [[PubMed](#)]
46. Kawai, H.; Nagata, M.; Kageyama, H.; Tukamoto, A.R.; West, A. New Lithium Cathode LiCoMnO_4 : Toward Practical 5 V Lithium Batteries. *Electrochem. Solid State Lett.* **1998**, *1*, 212. [[CrossRef](#)]
47. Hu, M.; Tian, Y.; Su, L.; Wei, J.; Zhou, Z. Preparation and Ni-doping effect of nanosized truncated octahedral LiCoMnO_4 as cathode materials for 5 V li-ion batteries. *ACS Appl. Mater. Interfaces* **2013**, *5*, 12185–12189. [[CrossRef](#)]
48. Lin, H.-F.; Tsai, Y.R.; Cheng, C.-H.; Cheng, S.T.; Chen, D.Z.; Wu, N.-Y. Structural and electrochemical properties of LiCoMnO_4 doped with Mg, La, and F as a high-voltage cathode material for lithium ion batteries. *Electrochim. Acta* **2022**, *427*, 140904. [[CrossRef](#)]
49. Yang, Z.; Zhang, W.; Wang, Q.; Song, X.; Qian, Y. Synthesis of porous and hollow microspheres of nanocrystalline Mn_2O_3 . *Chem. Phys. Lett.* **2006**, *418*, 46–49. [[CrossRef](#)]
50. Li, Q.; Li, G.; Fu, C.; Luo, D.; Fan, J.; Xie, D.; Li, L. Balancing stability and specific energy in Li-rich cathodes for lithium ion batteries: A case study of a novel Li-Mn-Ni-Co oxide. *J. Mater. Chem. A* **2015**, *3*, 10592–10602. [[CrossRef](#)]
51. Feng, X.; Yang, Z.; Tang, D.; Kong, Q.; Gu, L.; Wang, Z.; Chen, L. Performance improvement of Li-rich layer-structured $\text{Li}_{1.2}\text{Mn}_{0.54}\text{Ni}_{0.13}\text{Co}_{0.13}\text{O}_2$ by integration with spinel $\text{LiNi}_{0.5}\text{Mn}_{1.5}\text{O}_4$. *Phys. Chem. Chem. Phys.* **2015**, *17*, 1257–1264.
52. Hong, J.; Seo, D.H.; Kim, S.W.; Gwon, H.; Oh, S.T.; Kang, K. Structural evolution of layered $\text{Li}_{1.2}\text{Ni}_{0.2}\text{Mn}_{0.6}\text{O}_2$ upon electrochemical cycling in a Li rechargeable battery. *J. Mater. Chem.* **2010**, *20*, 10179–10186. [[CrossRef](#)]
53. Yu, H.; Zhou, H. High-Energy Cathode Materials (Li_2MnO_3 - LiMO_2) for Lithium-Ion Batteries. *J. Phys. Chem. Lett.* **2013**, *4*, 1268–1280. [[CrossRef](#)] [[PubMed](#)]
54. Baddour-Hadjean, R.; Pereira, J.P. Raman Microspectrometry Applied to the Study of Electrode Materials for Lithium Batteries. *Chem. Rev.* **2010**, *110*, 1278–1319. [[CrossRef](#)]
55. Yi, L.; Liu, Z.; Yu, R.; Zhao, C.; Peng, H.; Liu, M.; Wu, B.; Chen, M.; Li-Rich, X.W. Layered/Spinel Heterostructured Special Morphology Cathode Material with High Rate Capability for Li-Ion Batteries. *ACS Sustain. Chem. Eng.* **2017**, *5*, 11–11005. [[CrossRef](#)]
56. Moses, A.W.; Flores, H.G.G.; Kim, J.G.; Langell, A.M. Surface properties of LiCoO_2 , LiNiO_2 and $\text{LiNi}_{1-x}\text{Co}_x\text{O}_2$. *Appl. Surf. Sci.* **2007**, *253*, 4782–4791. [[CrossRef](#)]
57. Treuil, N.; Labrugère, C.; Menetrier, M.; Portier, J.; Campet, G.; Deshayes, A.; Frison, J.-C.; Hwang, S.-J.; Song, S.-W.; Choy, J.-H. Relationship between Chemical Bonding Nature and Electrochemical Property of LiMn_2O_4 Spinel Oxides with Various Particle Sizes: “Electrochemical Grafting” Concept. *J. Phys. Chem. B* **1999**, *103*, 2100–2106. [[CrossRef](#)]

58. Peng, H.; Zhao, S.-X.; Huang, C.; Yu, L.Q.; Fang, Z.-Q.; Guo-Dan, W. In Situ Construction of Spinel Coating on the Surface of a Lithium-Rich Manganese-Based Single Crystal for Inhibiting Voltage Fade. *ACS Appl. Mater. Interfaces* **2020**, *12*, 11579–11588. [[CrossRef](#)]
59. Thackeray, M.M.; David, W.I.F.; Bruce, P.G.; Goodenough, B.J. Lithium insertion into manganese spinels. *Mater. Res. Bull.* **1983**, *18*, 461–472. [[CrossRef](#)]
60. Armstrong, A.R.; Holzapfel, M.; Novak, P.; Johnson, C.S.; Kang, S.-H.; Thackeray, M.M.; Bruce, P.G. Demonstrating Oxygen Loss and Associated Structural Reorganization in the Lithium Battery Cathode $\text{Li}[\text{Ni}_{0.2}\text{Li}_{0.2}\text{Mn}_{0.6}]\text{O}_2$. *J. Am. Chem. Soc.* **2006**, *128*, 8694–8698. [[CrossRef](#)]
61. Lim, J.-H.; Bang, H.; Lee, K.-S.; Amine, K.; Sun, Y.-K. Electrochemical characterization of Li_2MnO_3 - $\text{Li}[\text{Ni}_{1/3}\text{Co}_{1/3}\text{Mn}_{1/3}]\text{O}_2$ - LiNiO_2 cathode synthesized via co-precipitation for lithium secondary batteries. *J. Power Source* **2009**, *189*, 571–575.
62. Zheng, J.; Gu, M.; Xiao, J.; Zuo, P.; Wang, C.; Zhang, J.-G. Corrosion/fragmentation of layered composite cathode and related capacity/voltage fading during cycling process. *Nano Lett.* **2013**, *13*, 3824. [[CrossRef](#)] [[PubMed](#)]
63. Zheng, J.; Xiao, J.; Gu, M.; Zuo, P.; Wang, C.; Zhang, J.G. Interface modifications by anion receptors for high energy lithium ion batteries. *J. Power Source* **2014**, *250*, 313–318. [[CrossRef](#)]
64. Gu, M.; Belharouak, I.; Zheng, J.; Wu, H.; Xiao, J.; Genc, A.; Amine, K.; Thevuthasan, S.; Baer, D.R.; Zhang, J.-G.; et al. Formation of the Spinel Phase in the Layered Composite Cathode Used in Li-Ion Batteries. *ACS Nano* **2013**, *7*, 760–767. [[CrossRef](#)] [[PubMed](#)]
65. Mohanty, D.; Kalnaus, S.; Meisner, R.A.; Rhodes, K.J.; Li, J.L.; Payzant, E.A.; Wood, D.L.; Daniel, C. Structural transformation of a lithium-rich $\text{Li}_{1.2}\text{Co}_{0.1}\text{Mn}_{0.55}\text{Ni}_{0.15}\text{O}_2$ cathode during high voltage cycling resolved by in situ X-ray diffraction. *J. Power Sources* **2013**, *229*, 239. [[CrossRef](#)]
66. Fell, C.R.; Chi, M.; Meng, Y.S.; Jones, J.L. In situ X-ray diffraction study of the lithium excess layered oxide compound $\text{Li}[\text{Li}_{0.2}\text{Ni}_{0.2}\text{Mn}_{0.6}]\text{O}_2$ during electrochemical cycling. *Solid State Ion.* **2012**, *207*, 44. [[CrossRef](#)]
67. Qiu, B.; Zhang, M.H.; Xia, Y.G.; Liu, Z.P.; Meng, Y.S. Understanding and Controlling Anionic Electrochemical Activity in High-Capacity Oxides for Next Generation Li-Ion Batteries. *Chem. Mater.* **2017**, *29*, 908–915. [[CrossRef](#)]
68. Yan, P.F.; Nie, A.; Zheng, J.M.; Zhou, Y.G.; Lu, D.P.; Zhang, X.F.; Xu, R.; Belharouak, I.; Zu, X.A.; Xiao, J.; et al. Evolution of Lattice Structure and Chemical Composition of the Surface Reconstruction Layer in $\text{Li}_{1.2}\text{Ni}_{0.2}\text{Mn}_{0.6}\text{O}_2$ Cathode Material for Lithium Ion Batteries. *Nano Lett.* **2015**, *15*, 514–522. [[CrossRef](#)]
69. Ye, D.L.; Zeng, G.; Nogita, K.; Ozawa, K.; Hankel, M.; Searles, D.J.; Wang, L.Z. Understanding the Origin of Li_2MnO_3 Activation in Li-Rich Cathode Materials for Lithium-Ion Batteries. *Adv. Funct. Mater.* **2015**, *25*, 7488–7496. [[CrossRef](#)]
70. Wu, F.; Liu, J.R.; Li, L.; Zhang, X.X.; Luo, R.; Ye, Y.S.; Chen, R.J. Surface Modification of Li-Rich Cathode Materials for Lithium-Ion Batteries with a PEDOT:PSS Conducting Polymer. *ACS Appl. Mater. Interfaces* **2016**, *8*, 23095–23104. [[CrossRef](#)]